JOURNAL OF SYNCHROTRON RADIATION

ISSN 1600-5775

Very high brightness and power LCLS-II hard X-ray pulses

Aliaksei Halavanau,[a,b]* Franz-Josef Decker,[a] Claudio Emma,[a] Jackson Sheppard[a] and Claudio Pellegrini[a]

[a]SLAC National Accelerator Laboratory, Menlo Park, CA, USA, and [b]University of California, Los Angeles, CA, USA. *Correspondence e-mail: aliaksei@slac.stanford.edu

Received 11 December 2018
Accepted 18 February 2019

Edited by A. F. Craievich, University of São Paulo, Brazil

Keywords: FEL; fresh-bunch FEL; terawatt FEL.

The feasibility of generating X-ray pulses in the 4–8 keV fundamental photon energy range with 0.65 TW peak power, 15 fs pulse duration and 9×10^{-5} bandwidth using the LCLS-II copper linac and hard X-ray (HXR) undulator is shown. In addition, third-harmonic pulses with 8–12 GW peak power and narrow bandwidth are also generated. High-power and small-bandwidth X-rays are obtained using two electron bunches separated by about 1 ns, one to generate a high-power seed signal, the other to amplify it through the process of the HXR undulator tapering. The bunch delay is compensated by delaying the seed pulse with a four-crystal monochromator. The high-power seed leads to higher output power and better spectral properties, with more than 94% of the X-ray power within the near-transform-limited bandwidth. Some of the experiments made possible by X-ray pulses with these characteristics are discussed, such as single-particle imaging and high-field physics.

1. Introduction

In this paper, we consider using the LCLS-II copper linac and the variable-gap hard X-ray (HXR) undulator to implement the double-bunch free-electron laser (DBFEL) concept (Ding *et al.*, 2010*a*; Geloni *et al.*, 2010; Emma *et al.*, 2017*a*). In the paper by Emma *et al.* (2017*a*) the DBFEL was mainly studied for the generation of high-power harmonics. In this paper we study its use to increase the fundamental peak power and X-ray brightness. We also compare the results with those of other self-seeding methods, such as single-bunch (Amann *et al.*, 2012) and fresh-slice self-seeding (Lutman *et al.*, 2016, 2018; Emma *et al.*, 2017*b*), showing that the DBFEL gives the highest peak power and brightness at LCLS-II.

The DBFEL is equivalent of having two FELs, the first to generate a high-power, small-bandwidth, seeding signal and the second to amplify it. The main advantage with respect to other LCLS self-seeding schemes using a single bunch is to have large seed power and pulse energy within a small bandwidth, leading, as we will show in Section 6, to larger output power and better spectral properties, and thus a large improvement in the X-ray peak brightness of LCLS-II. Comparing with fresh-slice self-seeding, DBFEL has the advantage of using for the same pulse duration electron bunches with a smaller charge and hence a smaller emittance.

This concept can be implemented in LCLS-II using two bunches from the copper linac, separated in time by about 1 ns, and a four-crystal monochromator to delay the seed pulse by the same amount of time. Using this scheme the seed signal for the amplifier is an order of magnitude or more larger than in other single-bunch self-seeding systems, an important advantage leading to increased output power and improved

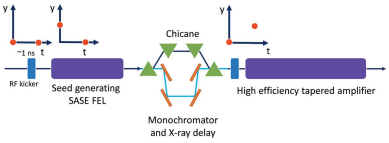

longitudinal coherence, as we will show in this paper. The HXR variable-gap undulator allows strong tapering and high efficiency of energy transfer from the electron beam to the radiation field. The acceleration of multiple bunches in the linac, with variable time separation, needed for the double-bunch system has already been achieved on the SLAC copper linac (Decker *et al.*, 2010).

In this paper, we first show the results of time-dependent *GENESIS* (Reiche, 1999) simulations of the double-bunch FEL using standard LCLS operating electron beam parameters. We compare, for the same beam parameters, the X-ray pulse characteristics for the proposed DBFEL with those of the single-bunch, single-crystal self-seeding system presently in operation (Amann *et al.*, 2012). The paper is organized as follows. In Section 2 we consider in detail the DBFEL system and the generation of the seed signal. In Section 3 we discuss the amplifier section tapering strategy, in Section 4 the monochromator design and properties, and in Section 5 the system to generate the two bunches and control their relative timing and energy. In Section 6 we present and discuss our main results on the radiation generated in the range 4–8 keV. In Section 6.3 we provide a quantitative comparison of DBFEL with the existing fresh-slice technique, based on experimental LCLS performance. Finally, in Section 7 we discuss some of the applications made possible by the availability of near-TW X-ray pulses such as single-particle imaging (Aquila *et al.*, 2015; Sun *et al.*, 2018*b*; Geloni *et al.*, 2012). We also consider the possibility of focusing the photons to a spot size of 10 nm, smaller than the present value of 100 nm, for high-field science. We notice that the power density obtained with a 10 nm spot size is about 2×10^{23} W cm^{-2}, and the corresponding peak electric field value is 10^{15} V m^{-1}.

This value is larger or comparable with that obtainable with PW lasers becoming available in a few laboratories. Thus a DBFEL would open the possibility of exploring high-field science in the X-ray wavelength region, complimentary to PW lasers in the micrometre wavelength region.

2. High-power double-bunch FEL

A schematic of a double-bunch FEL is shown in Fig. 1. In the first undulator section we let the first bunch lase, generating a large power, possibly reaching saturation. In the process the bunch energy spread grows to the order of the FEL parameter, about 10^{-3}, precluding its use in the amplifier section. The second bunch goes through the first undulator section with a large oscillation around the axis, produced by a transverse electric field cavity, and does not lase, accumulating negligible increase in its energy spread (Baxevanis *et al.*, 2017). At the exit of the first undulator section the first bunch is kicked out, and the second bunch receives a counter kick to move on axis in the following undulator. The radiation field is filtered through a monochromator and delayed by a time equal to the separation between the two bunches. The chicane is then used for the electron beam to bypass the monochromator crystals. At the entrance of the tapered undulator section, the second bunch is seeded and amplified.

The two undulators, soft X-ray (SXR) and hard X-ray (HXR), will be available for LCLS-II and are shown in Fig. 2. Their main properties are given elsewhere (Nuhn, 2011; Stohr, 2011; Lauer *et al.*, 2018) and summarized in Tables 1 and 2. We consider only the HXR undulator, with 32 sections, undulator period 2.6 cm, section length 340 cm, variable gap with an undulator parameter in the range of 2.4 to less than 1. The gap height can be adjusted longitudinally, giving a magnetic field change of up to 1% from the entrance to the exit and allowing for a smooth tapering profile (Nuhn, 2011). The separation between undulator sections is 60 cm, and two sections, 24 and 32,

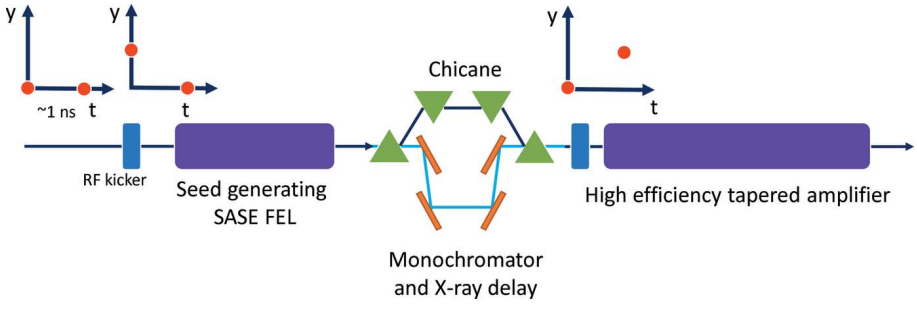

Figure 1
Schematic of a double-bunch LCLS-II undulator operation.

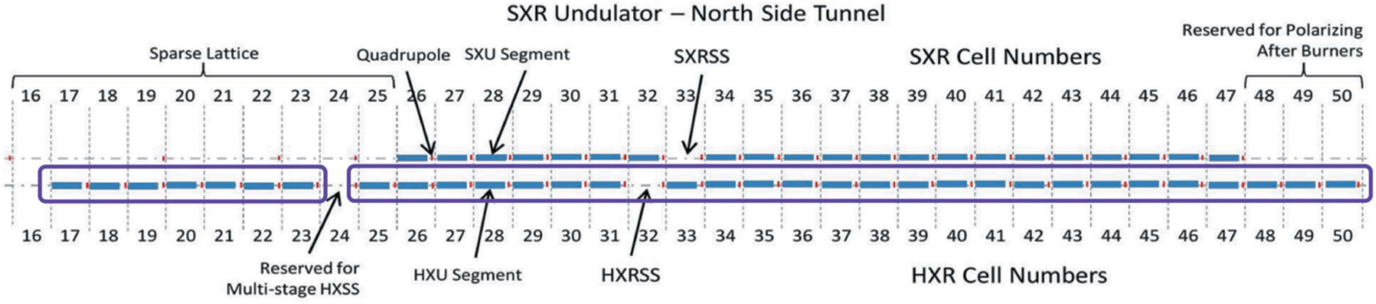

Figure 2
Schematic of LCLS-II variable-gap undulators. We propose to use the hard X-ray (HXR) undulator in the double-bunch configuration, inserting a four-crystal monochromator in section U24 (Nuhn, 2011).

Table 1
Beam parameters of the LCLS copper linac.

Parameter	Value
Electron beam energy, E	2.5–15 GeV
Electron bunch charge, Q_b	0.02–0.3 nC
Final r.m.s. bunch length, σ_z	0.5–52 μm
Peak current, I_{pk}	0.5–4.5 kA
Normalized transverse emittance, $\gamma\varepsilon_\perp$	0.2–0.7 μm
Energy spread, σ_E	2 MeV
Slice energy spread (r.m.s.), σ_{E_s}	500–2000 keV

Table 2
LCLS-II undulator parameters.

Parameter	SXR values	HXR values
Undulator period, λ_u	39 mm	26 mm
Segment length	3.4 m	3.4 m
Number of effective periods per segment, N_p	87	130
Minimum operating gap	7.2 mm	7.2 mm
Maximum K_{eff}	5.48	2.44
Maximum operating gap	22 mm	20 mm
Minimum K_{eff}	1.24	0.44

have a chicane for the electron beam and can be used to insert a single-crystal or a multiple-crystals monochromator. To minimize changes in the LCLS-II layout, we assume a four-crystal monochromator to be placed in section 24, use the first seven sections to generate the seed signal in a SASE mode and the remaining sections, U25 to U50, to amplify the seed. The general characteristics of the copper linac, based on the operational experience of LCLS, are given in Table 1.

We assume that the linac generates a flat current profile bunch (Ding *et al.*, 2016) to optimize the FEL performance. This is done by starting with a larger charge and bunch length and cutting its central part with collimators in the linac bunch compressor. In the case of Table 3 one starts with an 80 pC charge, reduced to 60 pC after collimation. The emittance, which depends on the charge, is evaluated at 80 pC to be 0.35 μm (Ding *et al.*, 2010*b*) and we increase this value to 0.4 μm in Table 3, to be on the conservative side. Note that for a later comparison with the double-slice FEL we use a bunch charge of 180 pC, corresponding to an initial charge of 240 pC and a normalized emittance of 0.6 μm.

We consider first the SASE undulator and evaluate the power gain length and peak power for two different energies and undulator parameter varying between 1 and 2.4. The results, obtained using Ming Xie's code (Xie, 1995, 2000) and for the electron beam parameters of Table 3, are shown in Figs. 3 and 4.

Using the first seven undulator sections to generate the seed, the useful undulator length is 23.8 m. It is possible to extend the photon energy range where SASE saturation is reached by moving the monochromator to section U27 or later; see Figs. 3 and 4. However, in this paper, we first discuss the LCLS-II performance without making any hardware changes and considering initially lasing in the range 4–8 keV, without reaching saturation in the initial SASE undulator section. The peak power profile, bunching and energy spread,

Table 3
Beam parameters for the double-bunch FEL performance evaluation at 4–8 keV.

Parameter	Value
Electron beam energy, E	6.5–9.25 GeV
Peak current, I_{pk}	4 kA
Normalized transverse emittance, $\gamma\varepsilon_\perp$	0.4 μm
Energy spread, σ_E	2 MeV
Average undulator beta, $\beta_\perp$	10 m
Bunch charge, Q	60 pC
Bunch duration, τ	15 fs

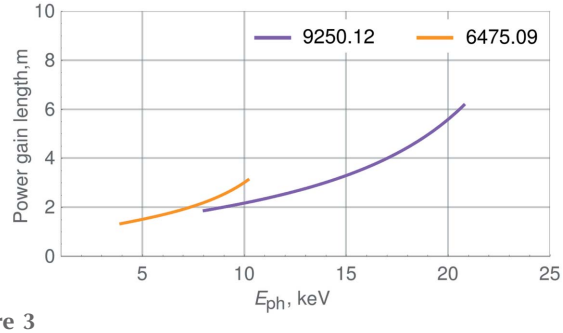

Figure 3
Power gain length as a function of photon energy for two different electron beam energies, in MeV, and for an undulator parameter varying between 1 and 2.4.

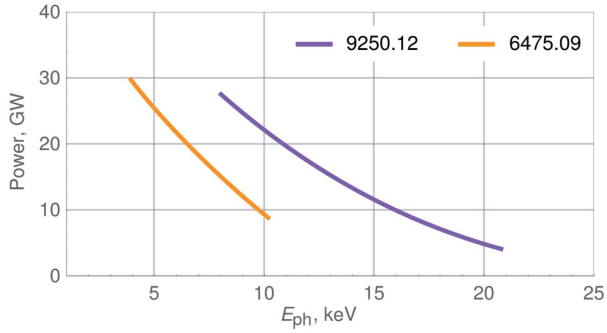

Figure 4
Saturation power as a function of photon energy for two different electron beam energies, in MeV, and for an undulator parameter varying between 1 and 2.4.

in the first seven SASE undulator sections, U17 to U23, is obtained by running *GENESIS* in the time-dependent mode; see Figs. 5 and 6.

The peak power at the SASE undulator exit, which was used to evaluate the seed signal, is 6 GW at 4 keV and 350 MW at 8 keV, as shown in Figs. 5 and 6. An alternative setup where the monochromator is located at the U32 section, as shown in Fig. 2, can be used to increase the SASE power at saturation, and therefore provide a much larger seed signal. In this paper, we mainly discuss the first case, which requires the fewest modifications to the present LCLS-II design.

3. Undulator tapering strategy

In this section, we discuss how to optimize the tapering of the magnetic field in the amplifier section of the undulator, in

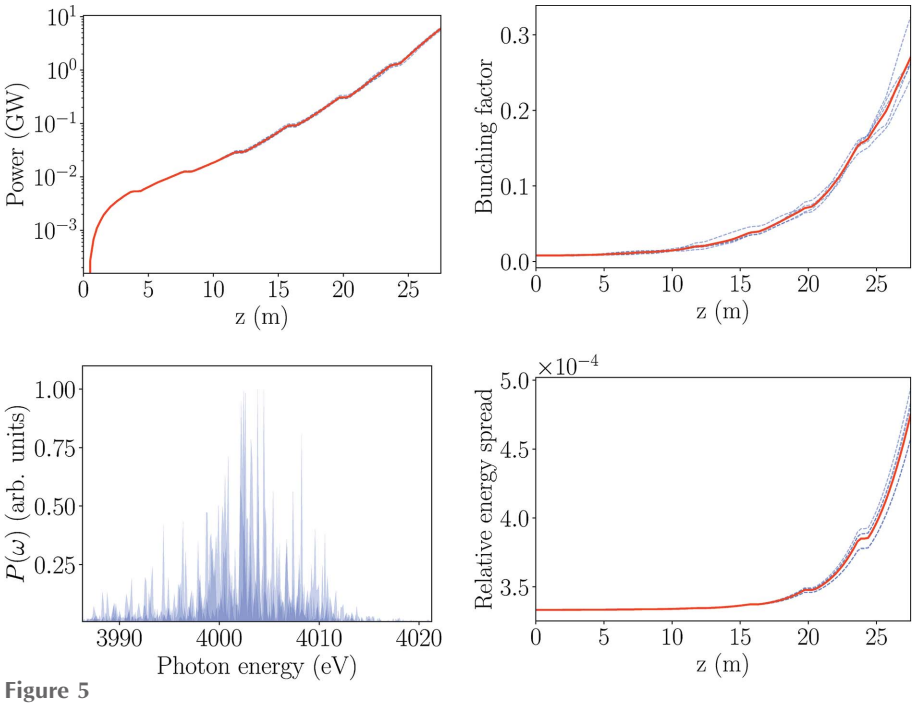

Figure 5
SASE section peak power, bunching, spectrum and energy spread for 4 keV photon energy. The peak output power at the exit of U23 is 6 GW. The red curves are average values over many initial noise distributions.

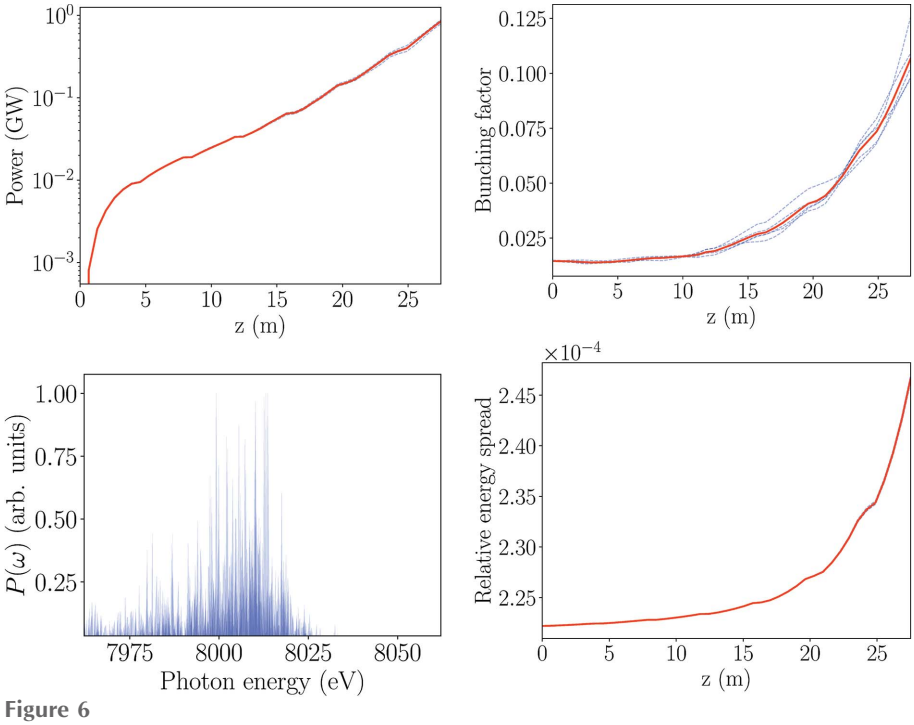

Figure 6
SASE section peak power, bunching, spectrum and energy spread for 8 keV photon energy. The peak output power at the exit of U23 is 350 MW. The red curves are average values over many initial noise distributions.

order to obtain a large energy transfer from the electron beam to the X-ray pulse. We note that it has been the subject of many studies since the seminal work of Kroll *et al.* (1981).

The magnetic field and the resonant phase ψ_r are adjusted in sections U25 to U50 to extract the maximum power using a local step-by-step optimization method. The resonant phase ψ_r, undulator parameter K and beam energy γmc^2 are related by

$$mc^2 \frac{d\gamma}{dz} = -\frac{eEK}{\gamma} \sin \psi_r, \qquad (1)$$

where E is the electric field acting on the electron. The beam energy and undulator parameter are also related by the synchronism condition

$$\lambda = \frac{\lambda_U (1 + K^2/2)}{2\gamma^2}, \qquad (2)$$

where λ is the photon wavelength and λ_U is the undulator period. The approach described here focuses on an *a priori* selection of the resonant phase profile along the tapered section of the undulator. With a pre-determined variation of the resonant phase, the change in the magnetic field can be calculated at each z-location in the undulator using the relationship (Pellegrini *et al.*, 2016)

$$\frac{dK}{dz} = -\frac{e}{mc^2} \frac{2\lambda}{\lambda_U} JJ(z)\, E(z) \sin \psi_r, \qquad (3)$$

where $JJ(z)$ is the difference of zeroth- and first-order Bessel functions,

$$JJ(z) = J_0\left[\frac{a_w^2}{2(1+a_w^2)}\right] - J_1\left[\frac{a_w^2}{2(1+a_w^2)}\right], \qquad (4)$$

and $a_w = K/\sqrt{2}$ is a function of z in the tapered section of the undulator. Here we assume that the average phase and energy of the electrons is the resonant energy and phase. The algorithm we use consists of computing the approximate numerical solution of equation (3) with the value of the electric field obtained from the *GENESIS* simulation at each z location. For the nth integration step, we have

$$K_{n+1} = K_n + \alpha_n E_n \sin \psi_{r,n} \qquad (5)$$

where

$$\alpha_n = -\frac{e}{mc^2} \frac{2\lambda}{\lambda_U} JJ_n(z)\, \Delta z.$$

Since the electrons are distributed across the bunch with non-zero radial extent, the amplitude of the electric field E is approximated as the field amplitude on-axis. Note that this approach is similar to the approach adopted in *GINGER*'s code self-design taper algorithm, which calculates the taper profile at each integration step for a pre-defined constant resonant phase (Fawley, 1995). Our method instead allows arbitrary variation of the

resonant phase along the undulator. This is similar to the approach discussed by Mak *et al.* (2017), Sudar *et al.* (2016) and Duris *et al.* (2015), but is not limited to expressing the resonant phase in the form of a polynomial function, as they assume in their papers.

The motivation for allowing arbitrary variation of ψ_r along the undulator is due to the fact that output power depends on the trade-off between the energy loss due to the FEL interaction ($d\gamma/dz \propto \sin\psi_r$) and the fraction of electrons trapped f_t. In the simplified 1D limit this can be expressed as $P(z) \propto (f_t \sin\psi_r)^2$. This scaling suggests that in the 1D approximation the main trade-off when designing a tapered FEL is between the number of electrons trapped in the stable decelerating bucket and the speed at which the trapped electrons lose energy to the radiation field (Schneidmiller & Yurkov, 2015). This occurs in general because the trapping fraction decreases as the resonant phase and the deceleration gradient increase. The optimal performance is obtained by balancing these two effects.

For the simple case of a constant resonant phase, the optimal value of the resonant phase can be determined analytically and found to be $\psi_r = 40^\circ$ for a cold electron beam and 20° for a warm beam (Brau & Cooper, 1979; Emma *et al.*, 2017*c*). Furthermore, for undulators much longer than the Rayleigh length, the growth of the radiation spot-size during the post-saturation region decreases the effective bucket area in which electrons are trapped and continues to lose energy to the radiation field. These considerations must be taken into account when choosing a particular profile for the resonant phase.

In general, the resonant phase is chosen to initially follow an almost linear increase, followed by a slow growth around the location of exponential saturation in an undulator. Towards the end of the undulator the resonant phase can be increased more rapidly to extract as much energy as possible from the electrons. Although the trapping fraction decreases, there is no interest in keeping electrons trapped beyond the end of the undulator. An example of the magnetic field change along the undulator and corresponding bunching factor of the second bunch is shown in Fig. 7.

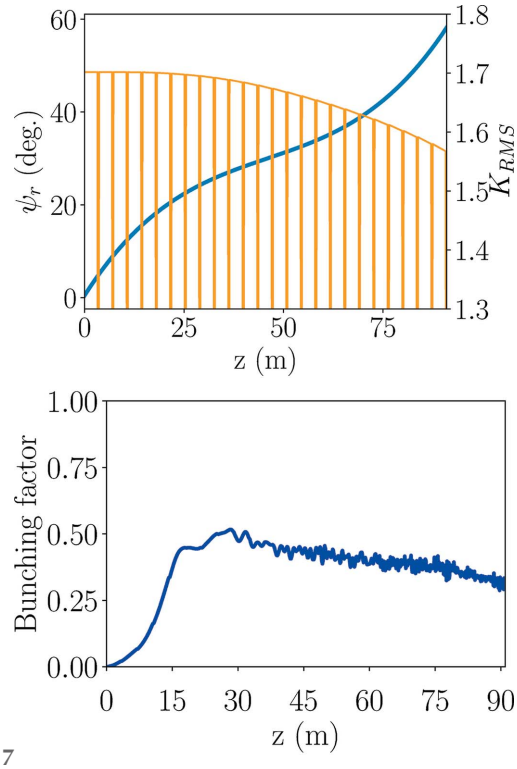

Figure 7
An example of an undulator K parameter profile along the undulator length (top panel) and corresponding evolution of the bunching factor (bottom panel) for 4 keV photons. The undulator parameter changes in the range between 1.7 and 1.57. The resonant phase ψ_r profile is plotted with a solid line and changes between 0 and 60°.

4. The four-crystal monochromator

A discussion about the four-crystal monochromator follows that of Emma *et al.* (2017*a*) but instead considers photon energies between 4 and 8 keV. The geometry is shown in Fig. 8. The X-ray photons' additional path length is given by

$$c\Delta t = 2h\tan\theta, \tag{6}$$

where θ is the Bragg angle and h is the lateral displacement.

For our monochromator crystals we choose diamond (1, 1, 1) crystals. At 4 keV the Bragg angle is $\theta = 48.8^\circ$ and the Darwin angle is 14.3 arcsec or about 71.5 µrad. This gives a bandwidth of $\Delta\lambda/\lambda = \tan^{-1}\theta\, d\theta \simeq 7.1 \times 10^{-5}$. The evaluation of the X-ray additional path length as a function of the lateral displacement h (see Fig. 8) is shown in Fig. 9. The reflectivity curves are shown in Fig. 10.

Alternative choices of crystal material are silicon, which has a bandwidth that is twice as large as that of diamond, or germanium, which is charaterized by very wide reflectivity window comparable with the SASE width. Both choices will result in multiple SASE modes passed to the amplifier and generate broader final spectral content (Lutman *et al.*, 2017).

The SASE signal bandwidth is about 2×10^{-3} (see Fig. 5) with 95% reflectivity and 7×10^{-5} bandwidth. The seed power, starting from 6 GW peak power at the exit of the first seven undulator sections, is reduced to 150 MW (efficiency of 2.5%). The seed power reduction at 8 keV is similar.

As shown in Table 4 and Fig. 10, the four-crystal monochromator based on diamond (1, 1, 1) crystals covers the full energy range from 4 to 8 keV with about the same photon energy acceptance. It provides continued tunability of the X-ray pulse in this energy range by rotating the crystals and

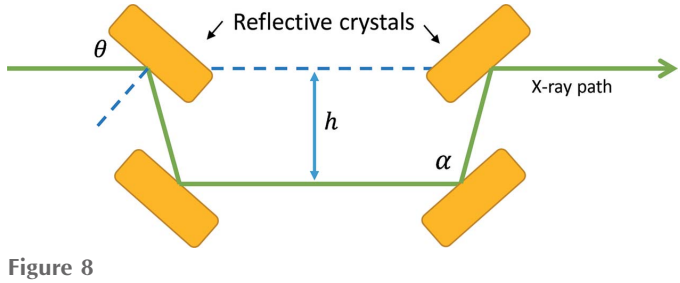

Figure 8
Geometry of the four-crystal monochromator.

Table 4
Bragg angle, Darwin width and photon energy acceptance for diamond (1,1,1) at 4 and 8 keV fundamental X-ray photon energy.

E_{ph} (keV)	Bragg angle	Darwin width (μrad)	$\Delta\omega/\omega$	Efficiency (%)
4	48.8	71	7.1×10^{-5}	2.5
8	22.1	25	6.2×10^{-5}	2.5

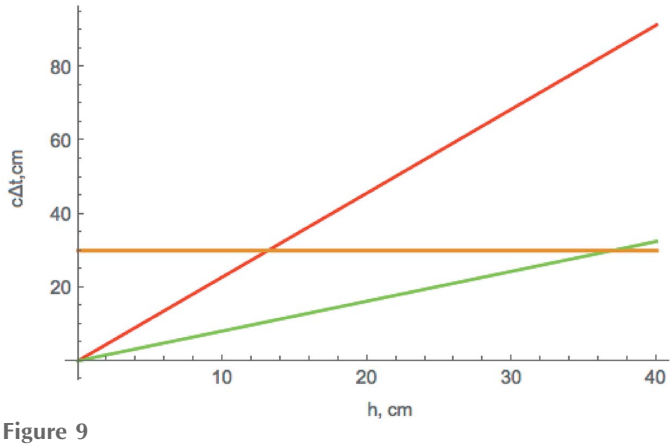

Figure 9
X-ray pulse delay in the four-crystal monochromator as a function of the lateral crystal displacement, h. For 1 ns we obtain h = 13 cm at 4 keV (red curve) and h = 37 cm at 8 keV (green curve).

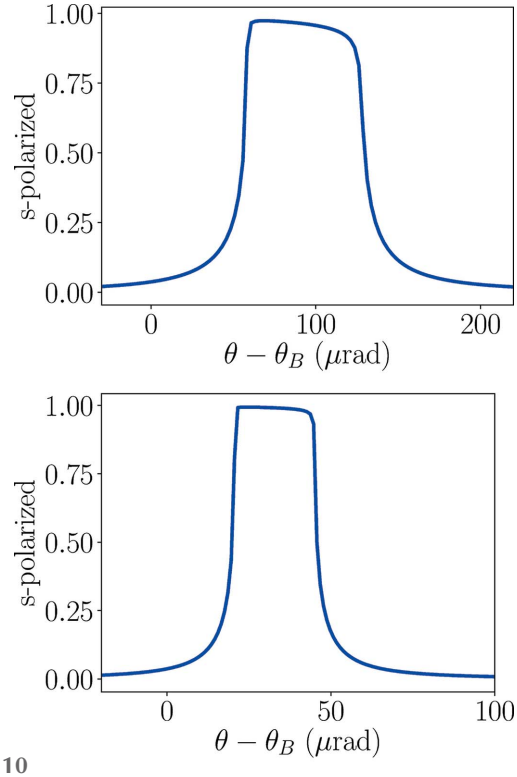

Figure 10
Diamond (1,1,1) reflectivity curves at 4 keV (top panel) and 8 keV (bottom panel) photon energy obtained using the *XOP* code (Sanchez del Rio & Dejus, 2011).

simultaneously changing the lateral displacement h. Lower photon energies would require a different choice of crystals.

5. Present double-bunch LCLS linac operation

The SLAC copper linac driving LCLS normally operates with a single electron bunch per macropulse. It has been shown by Decker *et al.* (2010) that multiple bunches can be generated within the linac macro-pulse. The bunches are separated in time by a multiple of the linac RF frequency, with small variations useful to control their relative energy. In our study, we consider two bunches separated by three RF cycles, or 1.05 ns. The bunches are created by sending two light pulses from two independent lasers on the LCLS photo-injector cathode. Their relative charge difference can be controlled to about the 1% level and their individual time separation can be adjusted with a precision of 0.07 ps. Longitudinal and transverse wakefields generated by the first bunch act on the successive bunch. The beam loading (or longitudinal wakefield) is 70 V pC^{-1} m^{-1}. For a 1 km-long RF linac and 60 pC bunch charge, we expect the second bunch to be 4 MeV lower in energy, or 0.07% at 6 GeV beam energy. This can be compensated by having a 0.08° phase difference between the two bunches in the second section, L2, of the linac [6 GeV × (cos 35° − cos 35.08°) = 4 MeV]. The difference of 0.08% is also compensated by timing the global RF pulse, since 0.08% is about the ratio of the 1.05 ns separation divided by the 825 ns RF fill time. The transverse wakefield could be used to give the second bunch a kick to oscillate around the axis, as needed in the DBFEL scheme. However, for now we assume for simplicity to use a separate transverse RF cavity to give the transverse kick to the second bunch and to compensate the linac wakefield if needed. The transverse effects are strong and can reach orbit differences of 100 μm in the undulator, which would inhibit lasing of the second bunch if not corrected [see Fig. 3 of Decker *et al.* (2018)]. This separation due to wakefields can be used to adjust it to the desired transverse separation. Successful experiments have been carried out using two bunches, such as the 'probe–probe' method [see Table 1 of Decker *et al.* (2015)], where the photon energy is exactly the same going through a monochromator.

6. DBFEL performance characteristics

In this section we discuss the characteristics of the X-ray pulse at the seeded amplifier exit, for different photon energies, as a function of the seed power. Our study is based on numerical simulations using the 3D time-dependent code *GENESIS*. Here we considered the LCLS-II HXR undulator with a step of five undulator periods, evaluating K using equation (5). The X-ray seeded amplifier power output and spectrum are evaluated for the cases of an initial seed signal equivalent to the SASE noise, 10 kW, the case of a single electron bunch, and using a DBFEL. The SASE noise signal of about 10 kW represents the case when no monochromator is inserted, and hence provides a baseline of X-ray power for the selected tapering scheme.

We evaluated the DBFEL performance for 4 keV and 8 keV photon production, the two extremes of our range of interest. For our studies, we selected the resonance phase profile shown in Fig. 7, which can be analytically approximated by $\psi_r(z) = 1.3538z - 0.0231z^2 + 0.00017z^3$. Other ways to optimize the resonant phase profile have been discussed by Wu *et al.* (2017, 2018) and Tsai *et al.* (2018). Deep multi-objective optimization of the DBFEL scheme will be the main focus of a separate study. Hereafter we discuss the power output of the DBFEL based on our tapering strategy.

Additionally, we also compare the power output with that of an FEL operating in the 1D regime, driven by an electron beam with negligible energy spread, the most favorable case, given by (Yu & Wu, 2002)

$$P_{\rm coh}(z) = \frac{Z_0 K^2 JJ(z)^2 I_{\rm pk}^2 b^2 z^2}{32\sqrt{2}\pi\sigma^2\gamma^2}, \qquad (7)$$

where $I_{\rm pk}$ is the peak current and b is the bunching factor. In this equation one assumes the peak current to be dependent on z as $I_{\rm pk} = I_0 f_t(z)$, where $f_t(z)$ is the trapping fraction.

6.1. 4 keV photon case

Using the results of Sections 2 and 4 the seed power can be as high as 150 MW when using two bunches and the four-crystal monochromator. When we consider a single bunch the seed power is limited to 5 MW to avoid an additional energy spread increase.

The performance of the DBFEL for 4 keV photon production is presented in Fig. 11. For the case of DBFEL we obtain 650 GW peak power downstream of the amplifier, which for the flat-top bunch with a duration of 15 fs yields about 10 mJ peak energy. For the single-bunch case the power is two times smaller, 320 GW. The power spectra for the two cases and the power temporal profile along the bunch are given in Fig. 12. Note that we have a flat profile along the bunch, following our assumption, discussed in Section 2, that the bunch current profile that we generate is flat. The noise present in the power distribution along the bunch is due to the growth of the SASE signal along the undulator due to the intrinsic beam noise.

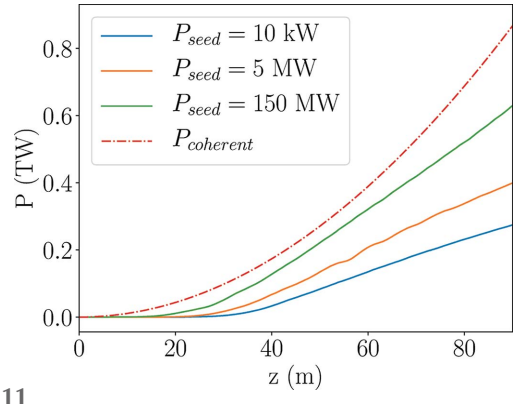

Figure 11
Amplifier undulator peak power output at 4 keV as a function of z compared with different seed power signals: 10 kW corresponds to the SASE noise case, 5 MW is the single-bunch seed power, and 150 MW is the maximum seed power for the two bunches case. The dashed line corresponds to the coherent power value given by equation (7) for the beam parameters provided in Table 3.

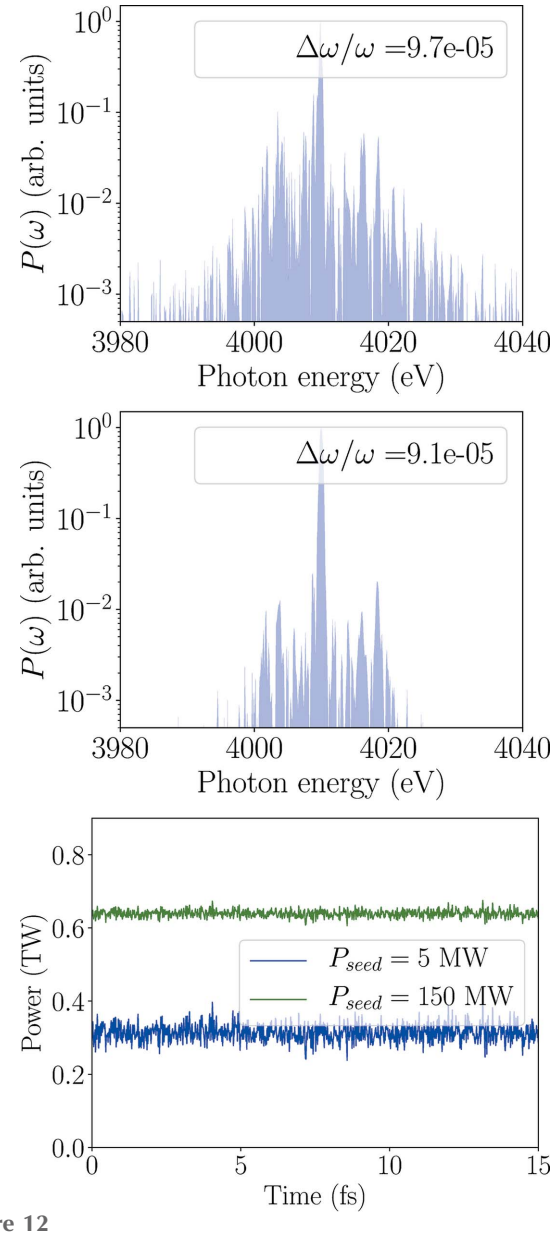

Figure 12
Power spectrum of 4 keV photons for the case of a single bunch (top panel) and the DBFEL (middle panel). X-ray power profile in the time domain (bottom panel).

One can see that the four-crystal monochromator yields a cleaner spectrum with relatively the same bandwidth. The amount of power stored in the fundamental harmonic for the DBFEL case is 92%, while for the single-bunch case it is about 82%. Correspondingly the temporal profile also improves for the DBFEL case. In summary, the DBFEL provides X-ray pulses with higher output peak power and more power stored in the main harmonic.

The third and fifth harmonics of the spectra obtained from non-linear harmonic generation are displayed in Fig. 13, showing again the advantage of the DBFEL.

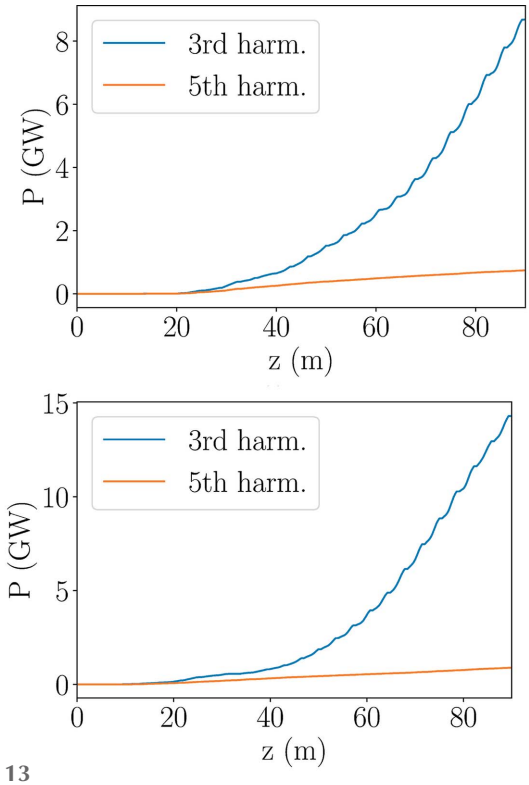

Figure 13
Third and fifth harmonics of 4 keV photons power as a function of z in the amplifier undulator for 5 MW (top panel) and 150 MW (bottom panel) input seed power.

6.2. 8 keV photon case

To establish the upper operating range of the DBFEL we consider the case of 8 keV photon production. Placing the four crystals at the U24 location the power output at the SASE section is 350 MW, as shown in Fig. 6, and the seed signal at the amplifier entrance is 5 MW. Moving the monochromator to section U27 increases the seed signal to 150 MW. We note that in this case for 4 keV photons we reach saturation and generate a 30 GW SASE signal, corresponding to 750 MW after the monochromator. We evaluated the DBFEL performance under these conditions and found that it remains essentially unchanged with respect to the case considered in the previous section.

The results of the simulations for the 8 keV case are shown in Figs. 14 and 15. For the 5 MW input seed case we obtain an output power of 135 GW, and for the 150 MW seed we obtain about 400 GW output power. When we account for the amplifier being three sections shorter, we obtain about 350 GW of power; see Fig. 14. The spectral harmonics are displayed in Fig. 15. For the case of a 150 MW input seed we have about 6 GW of power stored in the third harmonic at 24 keV, after reducing the amplifier length by three undulator sections. Finally, the power spectrum is presented in Fig. 16. The amount of power stored in the fundamental harmonic for the first case is 88% and for the latter case is 96%.

For the 8 keV case we have also evaluated the dependence of the output power on the seed power, as shown in Fig. 17. For the given beam parameters the output power starts to saturate at around 50 MW, corresponding to a peak SASE power of 2 GW, obtainable by moving the four-crystal monochromator by only two undulator sections.

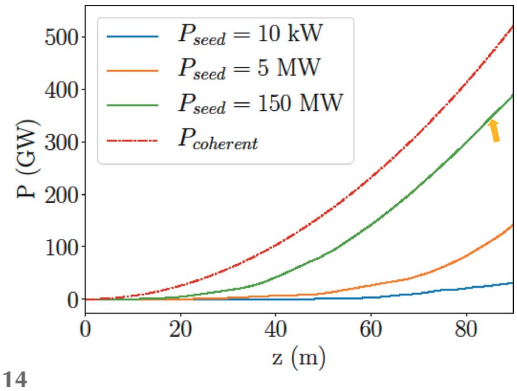

Figure 14
Amplifier undulator peak power output at 8 keV as a function of distance z compared with different seed power signals: 10 kW corresponds to the SASE case, 5 MW is the seed power for the four-crystal monochromator at U24 and 150 MW for the four-crystal monochromator at U27. The yellow arrow indicates the end of the HXR undulator in the latter case. The dashed line corresponds to the coherent power value given by equation (7) for the beam parameters provided in Table 3.

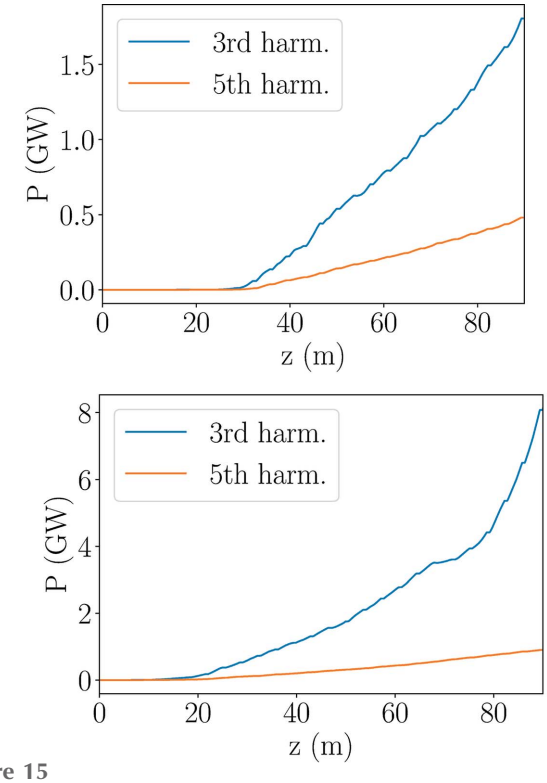

Figure 15
Third and fifth harmonics of the 8 keV photons power as a function of distance z in the amplifier undulator for 5 MW (top panel) and 150 MW (bottom panel) input seed power.

6.3. Comparison with double-slice self-seeding: energy spread and emittance effects

To evaluate the effects of the energy spread and emittance on the output power, we performed parametric scans for the cases of 4 keV and 8 keV photons; see Fig. 18. The results, as

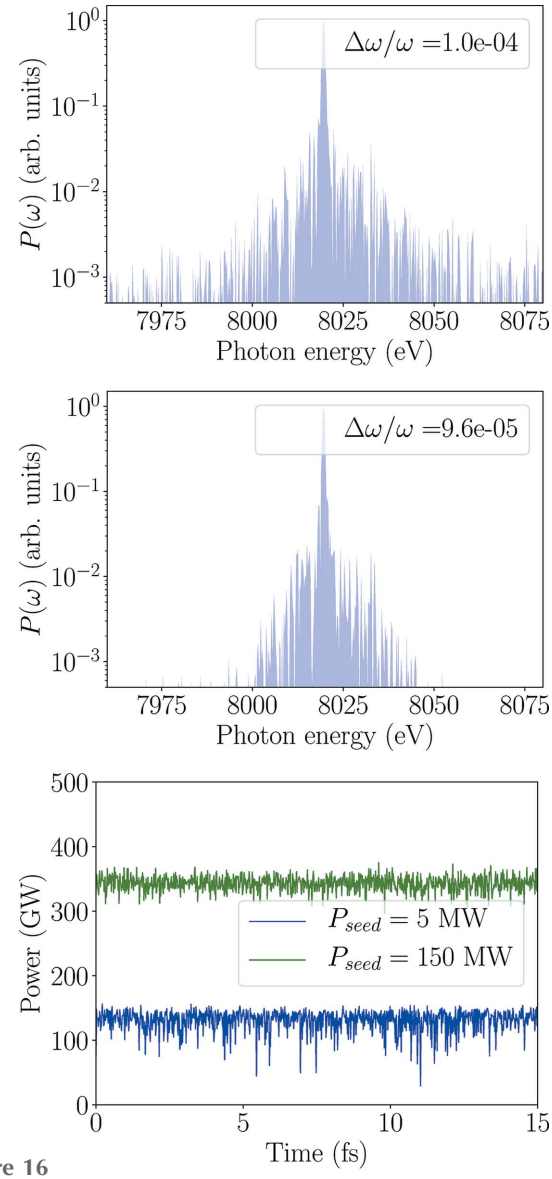

Figure 16
Power spectrum of 8 keV photons for the case of 5 MW input seed (top panel) and 150 MW input seed (middle panel) for the 8 keV photons. X-ray power profile in the time domain (bottom panel).

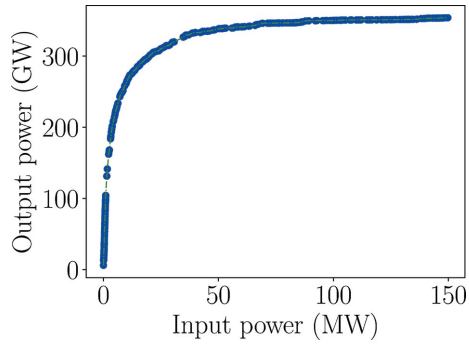

Figure 17
Output X-ray power as a function of input seed power for 8 keV photons.

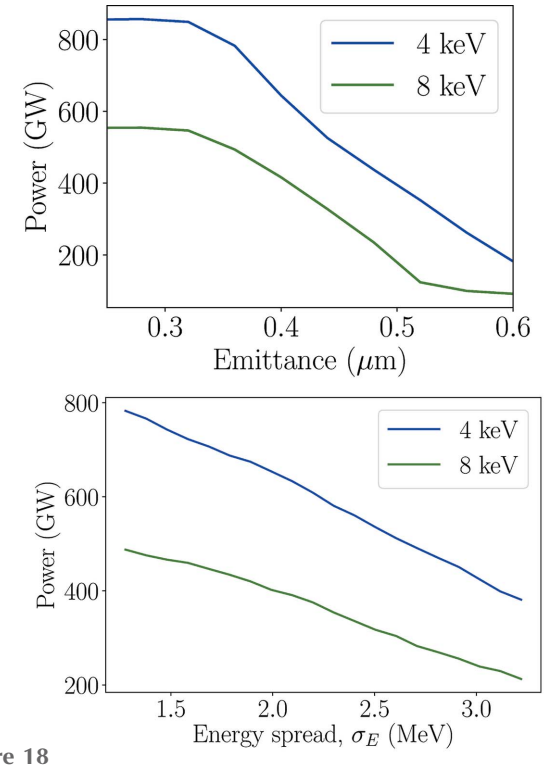

Figure 18
Output power as a function of transverse beam emittance (top panel) and energy spread of the second bunch (bottom panel).

expected, are strongly dependent on these two parameters. We notice that by decreasing the energy spread to 1.5 MeV or less the output power becomes equal to the coherent power in Figs. 11 and 14, proving this parameter to be of critical importance in determining the DBFEL performance. Fig. 18 also provides a comparison of the proposed DBFEL scheme with the existing double-slice single-bunch FEL (Emma *et al.*, 2017*a*), which already carries the brightness increase over the single-bunch case. In the double-slice configuration, only about one-third of the bunch is used to generate the SASE signal and another one-third for the amplification process. The remaining third of the bunch mostly contributes to the spectral background by increasing the overall beam emittance and the energy spread of the lasing slice (Craievich & Lutman, 2017). To compare this case with the DBFEL we must triple the charge from 60 pC to 180 pC, thus increasing the beam emittance from 0.4 µm to 0.6 µm (Ding *et al.*, 2010*b*). It can be seen from Fig. 18 that such an increase significantly lowers the X-ray output power, with respect to the DBFEL. Thus, with a minor change in the HXR beamline at higher photon energies, DBFEL far exceeds the double-slice FEL scheme. Alternatively, any possible enhancement in beam quality leads to even better performance of the DBFEL.

6.4. Shot-to-shot power fluctuations

To estimate shot-to-shot power fluctuations of 8 keV X-rays in our DBFEL setup we used the spectrum provided in Fig. 6 and the diamond (1,1,1) reflectivity curve shown in Fig. 10. To convert the reflectivity curve into the frequency domain we utilized the following relation, similar to Sun *et al.* (2018*a*),

$$\Delta\omega = -\omega \cot\theta_B \Delta\theta, \tag{8}$$

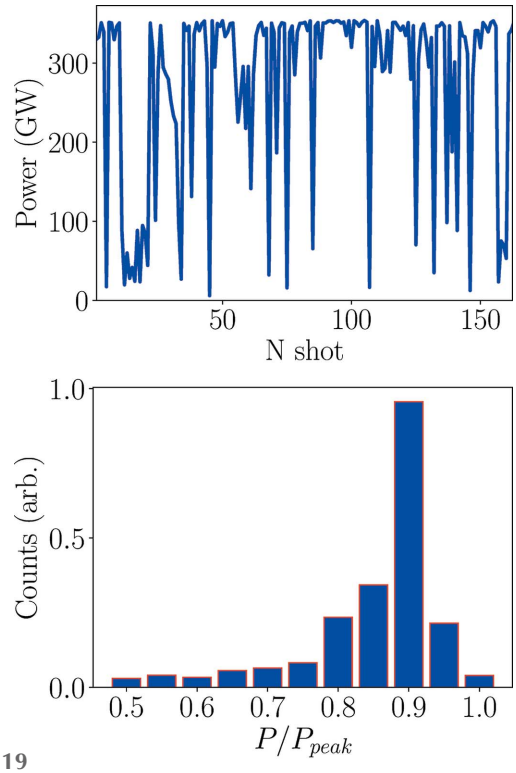

Figure 19
Shot-to-shot power fluctuations of 8 keV fundamental energy photons due to the SASE seed signal (top) and histogram of the power fluctuations (bottom).

where θ_B is the Bragg angle. For the cases of 4 and 8 keV photons we found the reflectivity window width to be similar to the single SASE spike width. Thus, we also note that the input seed signal can be assumed to be pseudo-Gaussian in time. To perform our calculations, we convoluted the SASE spectra and the crystal reflectivity curve directly for multiple realizations of SASE. The simulation results are presented in Fig. 19. As an effect of the tapering, the amplifier section is a very high gain system and saturates quickly, as displayed in Fig. 17. One can notice the significant fluctuations of the resulting X-ray power, corresponding to the very narrow bandwidth of the monochromator crystals.

The methods to reduce these fluctuations will be the topic of our future studies.

6.5. AGU undulator

For comparison and to better understand the effects of the undulator design, we also consider the possible use of the Advanced Gradient Undulator (AGU) (Emma *et al.*, 2016) as a second stage in our DBFEL system with the same beam parameters. In brief, the AGU is a proposed helical undulator based on a superconductor magnet technology and specifically designed for high X-ray power outputs. It is designed to have short drifts between undulator sections and provide strong electron beam focusing. We confine our studies to 8 keV fundamental photon energy. In this regime, we also consider two input seeds of 5 MW and 150 MW corresponding to the aforementioned cases of self-seeding. We confirm, via

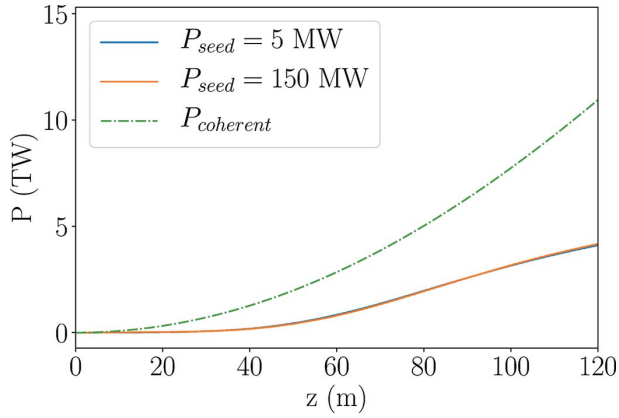

Figure 20
AGU undulator peak power output at 8 keV as a function of distance z compared with different seed power signals: 5 MW is the resulting four-crystal monochromator seed power at U24 and 150 MW signal for the four-crystal monochromator at U27. The dashed line corresponds to the coherent power value given by equation (7) for the beam parameters provided in Table 3.

numerical simulations, that AGU, embedded in the LCLS-II beamline, provides excellent X-ray output power in the multi-TW region using the DBFEL scheme, even at the low input power level, as one can see in Fig. 20. Note that the resonant phase profile was similar to that displayed in Fig. 7.

7. Applications of tapered DBFEL

In this section we consider a few applications of the high-power X-ray pulses generated in DBFEL. The applications are of course not limited to the ones discussed below. More applications will likely be developed once the system is in operation.

7.1. Single-particle imaging

An X-ray pulse of 4 keV photons with 650 GW output power and 15 fs pulse duration contains about 10 mJ of energy. This value corresponds to about 1.5×10^{13} coherent photons per pulse, a substantial increase with respect to what is achievable today and large enough for single-particle imaging (Aquila *et al.*, 2015). At 8 keV, and assuming an output power of 50 GW or larger, this number is reduced by a factor of three to 5×10^{12} coherent photons per pulse. We want to remember that our assumption on the beam characteristics are rather conservative and any operational improvement would lead to an even larger number of photons. It is also interesting to remark that this number would be largely increased in an AGU undulator. Lastly, we note that DBFEL can provide enough coherent photons for potential inelastic X-ray scattering experiments (Chubar *et al.*, 2016).

7.2. Strong field electrodynamics

The development of very high power lasers at about 1 μm wavelength, reaching the PW power region, has opened new capabilities for high-field science. These opportunities have been recently reviewed in a National Academy of Science

decadal report (Bucksbaum, 2018). X-ray FELs cannot reach the PW power level. However, the X-ray pulse can be focused to a much smaller spot size than the PW laser, tens of nanometres against a few to ten micrometres, yielding similar power density and peak electric field. The electric field gradient of $P_0 = 1$ TW X-rays focused to $\sigma_0 = 10$ nm spot is $E_0 = 1.2 \times 10^{15}$ V m^{-1} and the power density is $W_0 = 3.2 \times 10^{23}$ W cm^{-2}. The power density in W cm^{-2} scales as

$$W = \frac{P}{\pi\sigma^2} = 3.2 \times 10^{23} \frac{P/P_0}{(\sigma/\sigma_0)^2}, \tag{9}$$

while the electric field gradient in V m^{-1} scales as

$$E = \left(\frac{PZ_0}{\pi\sigma^2}\right)^{1/2} = 1.2 \times 10^{15} \frac{(P/P_0)^{1/2}}{(\sigma/\sigma_0)}, \tag{10}$$

where $P_0 = 1$ TW and $\sigma_0 = 10$ nm. We may view these numbers as reference and estimate the peak parameters of the tapered DBFEL. For the maximum of 650 GW of 4 keV photon peak power focused to a 100 nm spot size, a typical value presently obtainable, one obtains 2.1×10^{21} W cm^{-2} of power density and 9.6×10^{13} V m^{-1} field gradient. If possibly focused to a 10 nm spot size, a value recently achieved in a delicate state-of-the-art experiment at the SACLA XFEL facility in Japan (Mimura *et al.*, 2010; Yamauchi *et al.*, 2011), the 4 keV pulse obtained in a DBFEL gives a power density of 2×10^{23} W cm^{-2} and a peak electric field of 10^{15} V m^{-1}, values similar to those obtainable in a PW laser, as shown in Fig. 21 and by Pellegrini & Reis (2018). One can also consider backscattered HXR pulses that are additionally focused and collided head on with the electron beam, as was done in the E144 experiment at SLAC (Burke *et al.*, 1997).

In the electron rest frame the X-ray field gradient is multiplied by γ and the power density by γ^2, yielding for a 6 GeV electron beam and 100 µm X-ray spot size $W' = 3 \times 10^{29}$ W cm^{-2} and $E' = 1.2 \times 10^{18}$ V m^{-1}. If one recalls the Schwinger critical field gradient $E_{cr} = \alpha mc^2/er_e \simeq 1.3 \times 10^{18}$ V m^{-1} and $W_{cr} \simeq 4 \times 10^{29}$ W cm^{-2}, a DBFEL-generated X-ray signal backscattered with the electron beam can reach the regime where $E'/E_{cr} \equiv \chi \simeq 1$. In addition, with an improvement in X-ray focusing to a 10 nm spot size, if possible in the TW regime, one can reach $W' = 3 \times 10^{31}$ W cm^{-2}, $E' = 1.2 \times 10^{19}$ V m^{-1} and $\chi \simeq 10$, presenting an opportunity to probe perturbative and non-perturbative strong-field QED effects, currently unavailable at modern XFEL facilities. We note that for PW lasers the normalized vector potential a_0 is of the order of 1, while for X-rays it is smaller than 1, opening new and complimentary areas of exploration (Ritus, 1985; Di Piazza *et al.*, 2012; Mackenroth & Di Piazza, 2013). Hence, LCLS-II offers the possibility of exploring at X-ray wavelength most of the science that can be carried out with PW lasers, like laser–plasma interactions, high-energy-density science, planetary physics and astrophysics, and QED at extreme fields above the Schwinger limit.

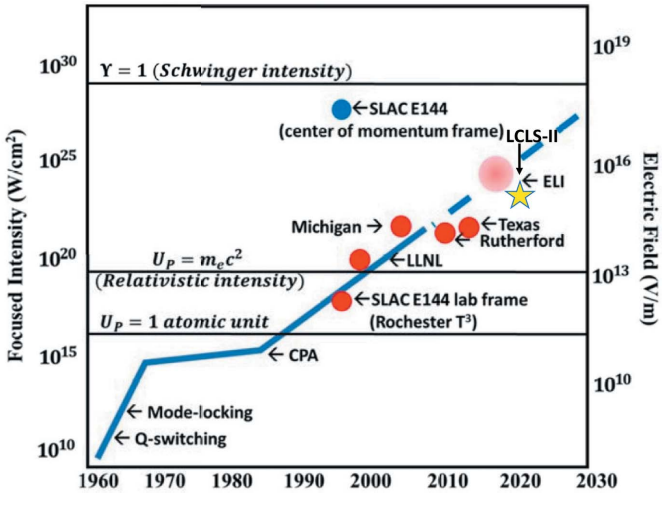

Figure 21
High-power lasers. Power density and peak electric field. The star represents LCLS-II in the DBFEL configuration and with the photon beam focused to a 10 nm spot size. Figure courtesy of P. Bucksbaum.

8. Conclusions

In conclusion, the presented DBFEL setup provides significant advantages over single-bunch and fresh-slice self-seeding schemes. We have demonstrated, via numerical simulations, that DBFEL can provide sub-TW X-ray pulses in the range of 4–8 keV with a nearly transform-limited spectrum bandwidth. Improvements in the beam quality and increase in the peak current make it possible to reach near 1 TW peak power level, which enables many new high-field physics experiments.

Acknowledgements

This work was supported by the US Department of Energy Contract No. DE-AC02-76SF00515. The authors are grateful to Yiping Feng, Yuantao Ding, Heinz-Dieter Nuhn, Juhao Wu, Zhirong Huang, Gennady Stupakov, Joe Duris, Gabriel Marcus, Chris Mayes, David Reis (SLAC) and Sebastian Meuren (Princeton University) for very useful and instructive discussions.

References

Amann, J., Berg, W., Blank, V., Decker, F.-J., Ding, Y., Emma, P., Feng, Y., Frisch, J., Fritz, D., Hastings, J., Huang, Z., Krzywinski, J., Lindberg, R., Loos, H., Lutman, A., Nuhn, H.-D., Ratner, D., Rzepiela, J., Shu, D., Shvyd'ko, Y., Spampinati, S., Stoupin, S., Terentyev, S., Trakhtenberg, E., Walz, D., Welch, J., Wu, J., Zholents, A. & Zhu, D. (2012). *Nat. Photon.* **6**, 693–698.

Aquila, A., Barty, A., Bostedt, C., Boutet, S., Carini, G., dePonte, D., Drell, P., Doniach, S., Downing, K. H., Earnest, T., Elmlund, H., Elser, V., Gühr, M., Hajdu, J., Hastings, J., Hau-Riege, S. P., Huang, Z., Lattman, E. E., Maia, F. R. N. C., Marchesini, S., Ourmazd, A., Pellegrini, C., Santra, R., Schlichting, I., Schroer, C., Spence, J. C. H., Vartanyants, I. A., Wakatsuki, S., Weis, W. I. & Williams, G. J. (2015). *Struct. Dyn.* **2**, 041701.

Baxevanis, P., Huang, Z. & Stupakov, G. (2017). *Phys. Rev. Accel. Beams*, **20**, 040703.

Brau, R. & Cooper, C. (1979). *Free-Electron Generators of Coherent Radiation*, edited by S. Jacobs, H. Pilloff, M. Sargent, M. Scully & R. Spitzer, p. 647. Reading: Addison-Wesley.

Bucksbaum, P. (2018). *Opportunities in Intense Ultrafast Lasers: Reaching for the Brightest Light.* Washington: The National Academies Press.

Burke, D. L., Field, R. C., Horton-Smith, G., Spencer, J. E., Walz, D., Berridge, S. C., Bugg, W. M., Shmakov, K., Weidemann, A. W., Bula, C., McDonald, K. T., Prebys, E. J., Bamber, C., Boege, S. J., Koffas, T., Kotseroglou, T., Melissinos, A. C., Meyerhofer, D. D., Reis, D. A. & Ragg, W. (1997). *Phys. Rev. Lett.* **79**, 1626–1629.

Chubar, O., Geloni, G., Kocharyan, V., Madsen, A., Saldin, E., Serkez, S., Shvyd'ko, Y. & Sutter, J. (2016). *J. Synchrotron Rad.* **23**, 410–424.

Craievich, P. & Lutman, A. A. (2017). *Nucl. Instrum. Methods Phys. Res. A*, **865**, 55–59.

Decker, F.-J., Akre, R., Brachmann, A., Ding, Y., Dowell, D., Emma, P. J., Fisher, A., Frisch, J., Gilevich, S., Hering, Ph., Huang, Z., Iverson, R. H., Loos, H., Messerschmidt, M., Nuhn, H.-D., Ratner, D. F., Schlotter, W. F., Smith, T. J., Turner, J. L., Welch, J. J., White, W. E. & Wu, J. (2010). *Proceedings of the 32nd International Free Electron Laser Conference (FEL2010)*, 23–27 August 2010, Malmo, Sweden, pp. 467–470. WEPB33.

Decker, F.-J., Bane, K., Colocho, W., Lutman, A. & Sheppard, J. (2018). *Proceedings of the 38th International Free Electron Laser Conference (FEL2017)*, 20–25 August 2017, Santa Fe, NM, USA, pp. 288–291. TUP023.

Decker, F.-J., Gilevich, S., Huang, Z., Loos, H., Marinelli, A., Stan, C., Turner, J., Van Hoover, Z. & Vetter, S. (2015). *Proceedings of the 37th International Free Electron Laser Conference (FEL2015)*, Daejeon, Korea, 23–28 August 2015, pp. 634–638. WEP023.

Ding, Y., Brachmann, A., Decker, F.-J., Dowell, D., Emma, P., Frisch, J., Gilevich, S., Hays, G., Hering, Ph., Huang, Z., Iverson, R., Loos, H., Miahnahri, A., Nuhn, H.-D., Ratner, D., Turner, J., Welch, J., White, W., Wu, J. & Pellegrini, C. (2010*b*). *Proceedings of the 23rd Particle Accelerator Conference (PAC'09)*, 4–May 2009, Vancouver, BC, Canada, pp. 2355–2357. WE5RFP040.

Ding, Y., Bane, K. L. F., Colocho, W., Decker, F.-J., Emma, P., Frisch, J., Guetg, M. W., Huang, Z., Iverson, R., Krzywinski, J., Loos, H., Lutman, A., Maxwell, T. J., Nuhn, H.-D., Ratner, D., Turner, J., Welch, J. & Zhou, F. (2016). *Phys. Rev. Accel. Beams*, **19**, 100703.

Ding, Y., Huang, Z. & Ruth, R. D. (2010*a*). *Phys. Rev. ST Accel. Beams*, **13**, 060703.

Di Piazza, A., Müller, C., Hatsagortsyan, K. Z. & Keitel, C. H. (2012). *Rev. Mod. Phys.* **84**, 1177–1228.

Duris, J., Murokh, A. & Musumeci, P. (2015). *New J. Phys.* **17**, 063036.

Emma, C., Fang, K., Wu, J. & Pellegrini, C. (2016). *Phys. Rev. Accel. Beams*, **19**, 020705.

Emma, C., Feng, Y., Nguyen, D. C., Ratti, A. & Pellegrini, C. (2017*a*). *Phys. Rev. Accel. Beams*, **20**, 030701–10.

Emma, C., Lutman, A., Guetg, M. W., Krzywinski, J., Marinelli, A., Wu, J. & Pellegrini, C. (2017*b*). *Appl. Phys. Lett.* **110**, 154101.

Emma, C., Sudar, N., Musumeci, P., Urbanowicz, A. & Pellegrini, C. (2017*c*). *Phys. Rev. Accel. Beams*, **20**, 110701.

Fawley, W. M. (1995). LBID-2141, CBP Technical Note-104, UC-414.

Geloni, G., Kocharyan, V. & Saldin, E. (2010). *arXiv*:1003.2548.

Geloni, G., Kocharyan, V. & Saldin, E. (2012). *arXiv*:1207.1981.

Kroll, N., Morton, P. & Rosenbluth, M. (1981). *IEEE J. Quantum Electron.* **17**, 1436–1468.

Lauer, K. R., Alarcon, A. D., Andrews, C. J., Babel, S., Bong, J. D., Boyes, M., D'Ewart, J. M., Levashov, Yu. I., Martinez-Galarce, D. S., McKee, B. D., Nuhn, H.-D., Petree, M., Rowen, M., Wolf, Z. R., Arbelaez, D., Bianculli, D., Brown, A. P., Corlett, J. N., DeMello, A. J., Garcia Fajardo, L., Jung, J.-Y., Leitner, M., Marks, S., McCombs, K. A., Munson, D. V., Ray, K. L., Sadlier, D. A., Wallén, E. J., Jansa, G., Oven, Z., Merritt, M. Smith, M. L. Voogd, R. J. & Xu, J. Z. (2018). *Proceedings of the 16th International Conference on Accelerator and Large Experimental Physics Control Systems (ICALEPCS 2017)*, Barcelona, Spain, 8–13 October 2017. THPHA020.

Lutman, A. A., Guetg, M. W., Maxwell, T. J., MacArthur, J. P., Ding, Y., Emma, C., Krzywinski, J., Marinelli, A. & Huang, Z. (2018). *Phys. Rev. Lett.* **120**, 264801.

Lutman, A., Huang, Z., Krzywinski, J., Wu, J., Zhu, D. & Feng, Y. (2017). *Proc. SPIE*, **10237**, 102370H.

Lutman, A. A., Maxwell, T. J., MacArthur, J. P., Guetg, M. W., Berrah, N., Coffee, R. N., Ding, Y., Huang, Z., Marinelli, A., Moeller, S. & Zemella, J. C. U. (2016). *Nat. Photon.* **10**, 745–750.

Mackenroth, F. & Di Piazza, A. (2013). *Phys. Rev. Lett.* **110**, 070402.

Mak, A., Curbis, F. & Werin, S. (2017). *Phys. Rev. Accel. Beams*, **20**, 119902.

Mimura, H., Handa, S., Kimura, T., Yumoto, H., Yamakawa, D., Yokoyama, H., Matsuyama, S., Inagaki, K., Yamamura, K., Sano, Y., Tamasaku, K., Nishino, Y., Yabashi, M., Ishikawa, T. & Yamauchi, K. (2010). *Nat. Phys.* **6**, 122–125.

Nuhn, H. D. (2011). Report No. SLAC-I060-003-000-07-R000. LCLS-II Conceptual Design Review. Linac Coherent Light Source, SLAC National Accelerator Laboratory, Menlo Park, CA, USA.

Pellegrini, C., Marinelli, A. & Reiche, S. (2016). *Rev. Mod. Phys.* **88**, 015006.

Pellegrini, C. & Reis, D. (2018). *Probing Strong-Field QED in Electron–Photon Interactions Workshop*, 21–24 August 2018, Hamburg, Germany (https://indico.desy.de/indico/event/19493/session/3/contribution/25).

Reiche, S. (1999). *Nucl. Instrum. Methods Phys. Res. A*, **429**, 243–248.

Rio, M. S. del & Dejus, R. J. (2011). *Proc. SPIE*, **8141**, 814115.

Ritus, V. I. (1985). *J. Russ. Laser Res.* **6**, 497–617.

Schneidmiller, E. A. & Yurkov, M. V. (2015). *Phys. Rev. ST Accel. Beams*, **18**, 030705.

Stohr, J. (2011). *LCLS-II Conceptual Design Report.* Linac Coherent Light Source, SLAC National Accelerator Laboratory, Menlo Park, CA, USA.

Sudar, N., Musumeci, P., Duris, J., Gadjev, I., Polyanskiy, M., Pogorelsky, I., Fedurin, M., Swinson, C., Kusche, K., Babzien, M. & Gover, A. (2016). *Phys. Rev. Lett.* **117**, 174801.

Sun, Y., Decker, F.-J., Turner, J., Song, S., Robert, A. & Zhu, D. (2018*a*). *J. Synchrotron Rad.* **25**, 642–649.

Sun, Z., Fan, J., Li, H. & Jiang, H. (2018*b*). *Appl. Sci.* **8**, 132.

Tsai, C.-Y., Emma, C., Wu, J., Yoon, M., Wang, X., Yang, C. & Zhou, G. (2018). *Nucl. Instrum. Methods Phys. Res. A*, **913**, 107–119.

Wu, J., Hu, N., Setiawan, H., Huang, X., Raubenheimer, T. O., Jiao, Y., Yu, G., Mandlekar, A., Spampinati, S., Fang, K., Chu, C. & Qiang, J. (2017). *Nucl. Instrum. Methods Phys. Res. A*, **846**, 56–63.

Wu, J., Huang, X., Raubenheimer, T. & Scheinker, A. (2018). *Proceedings of the 38th International Free Electron Laser Conference (FEL2017)*, 20–25 August 2017, Santa Fe, NM, USA, pp. 229–234. TUB04.

Xie, M. (1995). *Proceedings of the 1995 Particle Accelerator Conference (PAC95)*, 1–5 May 1995, Dallas, TX, USA, pp. 183–185. TPG10.

Xie, M. (2000). *Nucl. Instrum. Methods Phys. Res. A*, **445**, 67–71.

Yamauchi, K., Mimura, H., Kimura, T., Yumoto, H., Handa, S., Matsuyama, S., Arima, K., Sano, Y., Yamamura, K., Inagaki, K., Nakamori, H., Kim, J., Tamasaku, K., Nishino, Y., Yabashi, M. & Ishikawa, T. (2011). *J. Phys. Condens. Matter*, **23**, 394206.

Yu, L. & Wu, J. (2002). *Nucl. Instrum. Methods Phys. Res. A*, **483**, 493–498.